

# Tunnel junctions based on interfacial 2D ferroelectrics

Yunze Gao<sup>1,2</sup>, Astrid Weston<sup>1,2</sup>, Vladimir Enaldiev<sup>1,2</sup>, Eli Castanon<sup>1,2</sup>, Wendong Wang<sup>1,2</sup>,  
James E. Nunn<sup>3</sup>, Amy Carl<sup>1,2</sup>, Hugo De Latour<sup>1,2</sup>, Xiao Li<sup>1,2</sup>, Alex Summerfield<sup>1,2</sup>, Andrey  
Kretinin<sup>1,2</sup>, Nicholas Clark<sup>1,2</sup>, Neil Wilson<sup>3</sup>, Vladimir I. Fal'ko<sup>1,2,4,\*</sup> and Roman Gorbachev<sup>1,2,4,\*</sup>

**1** Department of Physics and Astronomy, University of Manchester, Oxford Road, Manchester, M13 9PL, UK

**2** National Graphene Institute, University of Manchester, Oxford Road, Manchester, M13 9PL, UK

**3** Department of Physics, University of Warwick, Coventry, CV4 7AL, UK

**4** Henry Royce Institute for Advanced Materials, University of Manchester, Oxford Road, Manchester, M13 9PL, UK

E-mail: vladimir.falko@manchester.ac.uk, roman@manchester.ac.uk.

*First three authors contributed equally.*

## Abstract

Van der Waals (vdW) heterostructures have opened new opportunities to develop atomically thin (opto)electronic devices with a wide range of functionalities. The recent focus on manipulating the interlayer twist angle has led to the observation of out-of-plane room temperature ferroelectricity in twisted rhombohedral (R) bilayers of transition metal dichalcogenides (TMDs). Here we explore the switching behaviour of sliding ferroelectricity using scanning probe microscopy domain mapping and tunnelling transport measurements. We observe well-pronounced ambipolar switching behaviour in ferroelectric tunnelling junctions (FTJ) with composite ferroelectric/non-polar insulator barriers and support our experimental results with complementary theoretical modelling. Furthermore, we show that the switching behaviour is strongly influenced by the underlying domain structure, allowing fabrication of diverse FTJ devices with various functionalities. We show that to observe the polarisation reversal, at least one partial dislocation must be present in the device area. This behaviour is drastically different from that of conventional ferroelectric materials and its understanding is an important milestone for future development of optoelectronic devices based on sliding ferroelectricity.

## Introduction

Ferroelectrics (FE) are a class of materials with the ability to maintain a spontaneous electric polarisation which can be switched by an external electric field. Due to this, ferroelectric materials have become the key element in devices for a broad range of electronic applications including sensors, capacitors, non-volatile memory, electro-optical switching and many others<sup>1</sup>. Room temperature FE devices are typically based on conventional bulk ferroelectrics, such as perovskites (e.g.  $\text{PbTiO}_3$ ,  $\text{BaTiO}_3$ ,  $\text{SrTiO}_3$ ), with a minimum thickness of a few nanometres<sup>2–6</sup>. While decreasing their thickness is desirable to reduce operating voltages and miniaturise their design, there are major challenges in engineering atomically thin metal-oxide ferroelectrics due to instability caused by depolarisation, interface chemistry and high contact resistances<sup>7</sup>.

2D materials are promising candidates for the next generation of (opto-)electronic devices with memory function due to their ultimate thickness limit and the lack of dangling bonds, making them immune to depolarisation<sup>8</sup>. In previous years, various groups have reported observations of intrinsic 2D in-plane ferroelectricity in materials such as (monolayer)  $\text{SnTe}$ <sup>9</sup>, and out-of-plane ferroelectricity in (d1T)  $\text{MoTe}_2$ <sup>10</sup>, (1T')  $\text{WTe}_2$ <sup>11</sup> few-layer (Td)  $\text{WTe}_2$ <sup>12</sup> and  $\text{CuInP}_2\text{S}_6$ <sup>13</sup>. More recently, engineering ferroelectric interfaces with broken inversion symmetry has opened a path to achieving interfacial ferroelectricity in twisted homo-bilayers of insulating  $\text{hBN}$ <sup>14–17</sup>, semiconducting transition metal dichalcogenides (TMDs) such as bilayer  $\text{MoS}_2$ ,  $\text{MoSe}_2$ ,  $\text{WSe}_2$  and  $\text{WS}_2$ <sup>17,18</sup>, as well as cumulative polarisation in multi-layer  $\text{MoS}_2$ <sup>19</sup>. In these studies, two thin crystals of 2D materials have been mechanically stacked with a small rotational misalignment (twist). This enables atomic reconstruction, resulting in large structural domains of alternating stacking order featuring broken inversion symmetry<sup>20</sup>. Due to asymmetric hybridization between the conduction band states in one layer and the valence band states in the other layer, charge transfer occurs between the layers producing a built-in electric field across the van der Waals gap. Such out-of-plane ferroelectric polarisation is bound to the underlying atomic structure of each domain, with switching enabled by the sliding movement of the partial dislocations separating reconstructed domains. While multiple applications of sliding ferroelectricity have been proposed<sup>8</sup>, an understanding of its switching behaviour in the context of electronic devices is still lacking.

Here, we study the polarization-dependent tunnelling electro-resistance (TER) in ferroelectric tunnel junction (FTJ) with a composite FE and non-polar dielectric barrier. To design the ferroelectric interface, we employ transition metal dichalcogenides which have recently been shown to display robust sliding ferroelectricity<sup>17,18</sup>, high crystalline and electronic quality<sup>21</sup>, as well as outstanding optical properties<sup>22</sup> widely considered necessary for next generation optoelectronic devices. We demonstrate unipolar

switching behaviour in the tunnelling current with ON/OFF ratios  $> 10$ . While methods of substantially increasing the ON/OFF ratio have been extensively demonstrated for conventional ferroelectrics<sup>1,3–6</sup>, here we focus on the switching behaviour instead, and show that it is remarkably different. We study multiple devices positioned over various shapes in the complex domain network and reveal a strong dependence of switching behaviour depending due to the nature of the local domain structure.

## Main Text

To produce the ferroelectric interface, two monolayers of MoS<sub>2</sub> have been transferred on top of each other with marginal twist angle using the tear-and-stamp process<sup>23</sup> and then placed onto an exfoliated graphite crystal. This process results in twist angle disorder (typically  $\pm 0.1^\circ$ <sup>24</sup>), a common feature of twisted bilayers assembled from isolated 2D crystals, as a consequence of the random strain produced during the transfer process. Here, the twist angle variation is more pronounced due to the use of a flexible polymer support in order to achieve a diverse domain network in each sample. An example of such a domain network visualised using lateral/friction-mode AFM with a conductive tip can be seen in Fig.1a. The bright and dark regions correspond to domains with different local stacking order, which we denote as Mo<sup>t</sup>S<sup>b</sup> (Mo atom in the top layer is aligned with S atom in the bottom layer) and S<sup>t</sup>Mo<sup>b</sup> (vice versa), Fig.1b. These structural domains possess opposite out-of-plane/perpendicular electrical polarisation with a ferroelectric potential of  $\Delta V_{FE} = \pm 63\text{mV}$  and can be locally switched by lateral migration of the partial dislocations separating the domains. Furthermore, the expansion and compression of the domains can be controlled by the applied external field<sup>20</sup>.

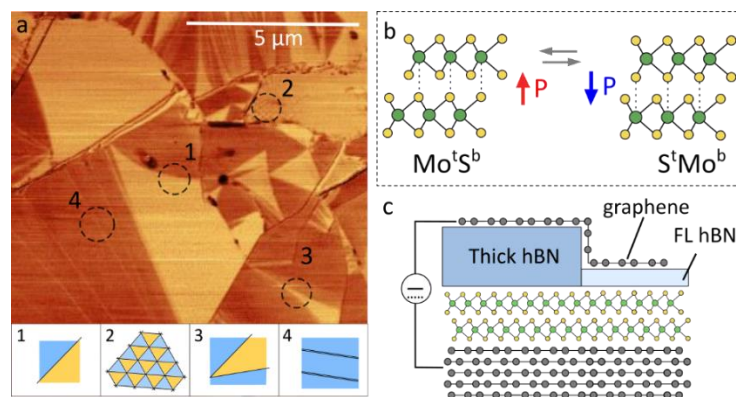


**Figure 1: Ferroelectric domains in rhombohedral MoS<sub>2</sub> bilayer:** (a) Contact mode friction AFM map of a marginally twisted bilayer sample on graphite with a variety of different domains present. Oppositely polarised Mo<sup>t</sup>S<sup>b</sup> and S<sup>t</sup>Mo<sup>b</sup> domains display clearly differentiated contrast. The black dashed circles highlight the 4 distinct domain geometries studied in this work, illustrated with matching schematics (bottom). (b) Schematics of the oppositely polarised Mo<sup>t</sup>S<sup>b</sup> and S<sup>t</sup>Mo<sup>b</sup> stacking configurations of the marginally twisted bilayer MoS<sub>2</sub> (R-MoS<sub>2</sub>). (c) Schematic of the ferroelectric tunnelling junction. The graphene source electrode is routed over thick (10–20 nm) hBN onto the region of interest, where the tunnelling junction with few-layer hBN and R-MoS<sub>2</sub> bilayer is formed.

Four characteristic domain configurations have been selected for device fabrication as highlighted with dashed circles in Fig.1a: **(1)** over a single partial dislocation between two large, roughly equal  $\text{Mo}^{\text{t}}\text{S}^{\text{b}}$  /  $\text{S}^{\text{t}}\text{Mo}^{\text{b}}$  domains; **(2)** over regular triangular domains with tens of nm period; **(3)** over three domains separated by domain walls; **(4)** similar configuration to (3) but with the middle domain fully collapsed into a perfect dislocation. The heterostructure was then covered by a few-layer hBN flake acting as a tunnelling barrier, a top graphene (source) electrode and a bottom graphite (drain) electrode, as shown in Fig.1c. The graphene electrode was selectively patterned producing small tunnelling contacts ( $\sim 500\text{nm}$ ) over the selected domain configurations 1-4, so that both tunnelling current and electric field switching behaviour can be studied locally. The resulting FTJs allow measuring a change in tunnelling current with the reversal of FE polarisation. The hBN tunnelling barrier serves to enhance FTJs performance<sup>25</sup> and protects the device by suppressing high tunnelling currents while allowing application of sufficient electric fields for FE switching.

The band diagram of the resulting system, corresponding to zero potential difference set between the source and drain electrodes ( $V_{\text{sd}}=0$ ) is shown in Fig.2a. Here, the conduction band of the  $\text{MoS}_2$  bilayer is  $U_{\text{MoS}} \approx 0.3$  eV above the Fermi level of graphite<sup>26</sup>, while the valence band of the hBN layer is  $U_{\text{BN}} \approx -2.66$  eV below the Dirac point of graphene as determined from complementary ARPES experiments (see SI Section 2). Due to the shortcut between the source and the drain, a small carrier density emerges in graphene and graphite to compensate for the contact potential difference ( $0.26\text{eV}$ <sup>27</sup>) between them, and to negate the FE potential from the rhombohedral  $\text{MoS}_2$  bilayer ( $\Delta_{\text{FE}} \approx 63$  meV<sup>28,29</sup>). This results in a corresponding electric field, so that the potential profile across the dielectric stack has an additional linear contribution equalising the electrochemical potentials  $\mu_1$  and  $\mu_2$ . Depending on the FE polarisation state of the  $\text{MoS}_2$  bilayer, the combined tunnelling barrier in both  $\text{MoS}_2$  and hBN can be switched to a lower or a higher state, which applies for both current directions. As the bias voltage is applied across the junction, Fig.2b,  $\sim 60\%$  of the total potential  $V_{\text{sd}}$  drops across the hBN (3L) and  $\sim 40\%$  in the  $\text{MoS}_2$  bilayer according to the ratio of dielectric constants and thicknesses of these materials. This behaviour persists up to a point where the  $\text{MoS}_2$  conduction band edge dips into the bias window at  $V_{\text{sb}} \sim 0.8$  V and the direct tunnelling into the bilayer becomes significant. This behaviour is indeed observed in devices where a single boundary is positioned roughly in the middle of the tunnelling contact (type 1).

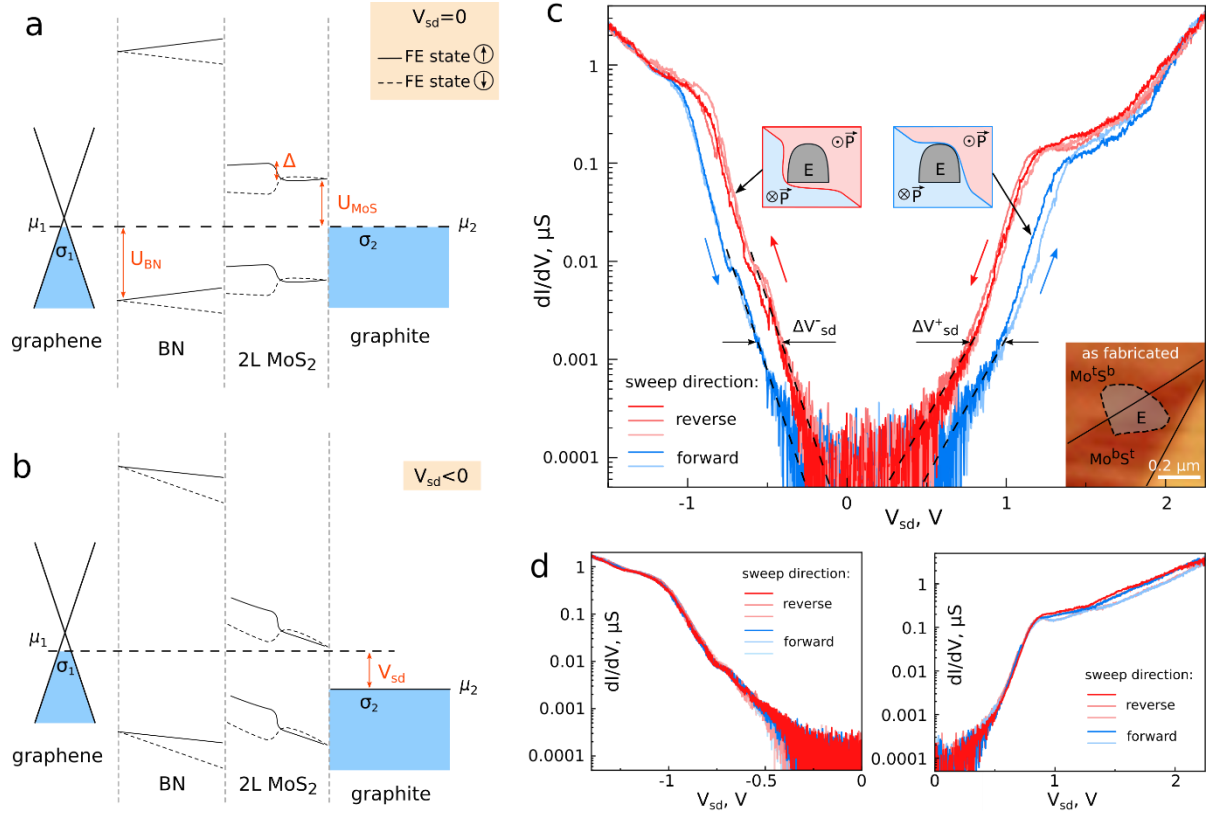


**Figure 2: Switching behaviour of FTJ over a  $\text{MoSb}/\text{S}'\text{MoS}$  dislocation (configuration 1) enabling full domain switching within the tunnelling area.** (a) Schematic band diagram with equipotential source and drain,  $V_{sd}=0$ . A small charge density  $\sigma$  is induced in graphene and graphite to cancel out the contact potential difference and ferroelectric potential from the rhombohedral  $\text{MoS}_2$  bilayer. Bold and dashed lines illustrate the potential profile created for upward and downward polarisation respectively. (b) Schematic band diagram when applying a small reverse bias  $V_{sd}$ , before the conduction band states of  $\text{MoS}_2$  become available for tunnelling. (c) Tunnelling conductance ( $dI/dV$ ) as a function of the transverse electric field ( $V_{sd}$ ) between the graphene source and the graphite drain. The direction of the  $V_{sd}$  sweeps is indicated by the arrows. Schematic insets show the domain configuration that produces the observed tunnelling behaviour, where the area of the FTJ electrode(E) is indicated in grey. In the bottom-right corner, a friction AFM map shows the existing domain configuration prior to the sweeps. For this device, the tunnelling hBN has a thickness of 3 layers. These results were acquired at  $T=1.5 \text{ K}$ . (d) Same as (c) but with the field only applied in one direction showing that no polarisation reversal is occurring within the sample. No hysteresis is observed in these cases.

In Figure 2c we plot the differential conductance in such a device, which shows clear hysteresis between the upwards and downwards directions of the applied field. It is important to note here that no hysteresis is observed until we increase the bias voltage above  $\pm 1.2 \text{ V}$ , corresponding to external electric fields  $\approx 0.55 \text{ V/nm}$ , above which significant domain wall movement is expected<sup>20</sup>. Therefore, the appearance of the pronounced switching at higher bias voltages can be attributed to the domain wall being fully expelled from the tunnelling area, creating a configuration where all the current flows through one polarised domain only. Once the  $V_{sd}$  drops below  $-1 \text{ V}$ , the opposite configuration is enabled, achieved by the reverse movement of the domain boundary across the tunnelling area and its expulsion on the other side, switching the FE polarisation in the entire device area. This is confirmed

by a substantial change in the tunnelling current threshold on the return curve, both for positive and negative currents,  $\Delta V_{sd}^+ \approx 0.170\text{mV}$  and  $\Delta V_{sd}^- \approx 0.140\text{mV}$ , respectively, which indicates a clear change in the tunnelling barrier height for different polarisations. The observed behaviour is consistent with the microscopic observations of the domain wall movement, where a substantial opposite field is required to completely reverse the domain layout<sup>20</sup>. The gradual movement of the domain wall across the device suggested by the absence of abrupt changes in the  $dI/dV$  characteristics is similar to conventional ferroelectric switching, where this phenomenon is attributed to disorder-controlled creep processes<sup>30</sup>. Consequently, if the voltage is repeatedly applied in one direction only (Fig.2d), the switching is not observed as the FE polarisation remains in the same state.

To understand the observed hysteresis behaviour, we model the FE tunnelling junction as a sequence of tunnel barriers with the profiles set by the band offsets and electric field distribution across the structure<sup>31</sup>,

$$I \propto \int_0^{-eV_{sd}} e^{-2S(\varepsilon)} d\varepsilon, \quad S(\varepsilon) = S_{MoS} + S_{BN}, \quad (1)$$

$$S_X = \int_0^{d_X} \sqrt{\frac{2m_X}{\hbar^2}} \sqrt{\varepsilon_{\pm,X}(z) - \varepsilon} dz, \quad X = MoS, BN.$$

Here, under the barrier action,  $S(\varepsilon)$  of a current carrier with energy  $\varepsilon$  is composed of contributions from hBN and MoS<sub>2</sub>, characterized by barrier profiles  $\varepsilon_{\pm,MoS}(z)$  and  $\varepsilon_{\pm,BN}(z)$  (see below), with " + " and " - " signs distinguishing two polarization states (Mo<sup>t</sup>S<sup>b</sup> and S<sup>t</sup>Mo<sup>b</sup>) of MoS<sub>2</sub> bilayer, and effective masses  $m_{MoS_2}$  and  $m_{BN}$ , respectively. In hBN we take into account that the valence band is much closer to the graphene's Fermi level than the conduction band, in contrast to MoS<sub>2</sub> where the conduction band is closer to the graphite's Fermi level. We also note that the band offsets relevant for the tunneling process are larger than the actual offsets of the valence band edge in hBN,  $-U_{BN}$ , and the conduction band edge in MoS<sub>2</sub>,  $U_{MoS}$ , as those crystals are not aligned/commensurate with the graphitic source and drain, so that tunneling through them involves arbitrary middle areas of their respective Brillouin zones away from band edge points. Because of this, we cannot uniquely quantify the value of the offsets for both materials ( $U_{BN} < 0$  and  $U_{MoS}$ ), as well as their out-of-plane effective masses for the conduction band states in MoS<sub>2</sub> ( $m_{MoS}$ ) and the valence band states in hBN ( $m_{BN} < 0$ ). Moreover, the absolute value of tunnelling transparency would additionally depend on the matching of the conduction/valence band states in MoS<sub>2</sub>/hBN at their interface and their contact with the graphitic electrodes.

Therefore, instead of attempting a detailed quantitative description of the  $I(V)$  characteristics, we focus on the qualitative trends related to the observed hysteresis behavior due to polarization switching. That is, we expand the barriers and their respective contributions towards the tunneling

action to the linear order of the bias field,  $\mathcal{F}_{\text{MoS}_2/\text{BN}}$ , in MoS<sub>2</sub>/BN and double layer potential ( $\pm\Delta$  for the two polarization states -- Mo<sup>t</sup>S<sup>b</sup> and S<sup>t</sup>Mo<sup>b</sup> -- of MoS<sub>2</sub> bilayer):

$$\varepsilon_{\pm, \text{MoS}} \left( z < \frac{d_{\text{MoS}}}{2} \right) = U_{\text{MoS}} + e\mathcal{F}_{\text{MoS}}z; \quad \varepsilon_{\pm, \text{MoS}} \left( z > \frac{d_{\text{MoS}}}{2} \right) = \varepsilon_{\pm, \text{MoS}}^{(c/v)} \left( z < \frac{d_{\text{MoS}}}{2} \right) \pm \Delta;$$

$$\varepsilon_{\pm, \text{BN}}(z) = U_{\text{BN}} + e\mathcal{F}_{\text{MoS}}d_{\text{MoS}} + e\mathcal{F}_{\text{BN}}(z - d_{\text{MoS}}) \pm \Delta,$$

determining the exponential dependence of I(V) characteristics as

$$\begin{aligned} \ln \left. \frac{dI}{dV_{\text{sd}}} \right|_{V_{\text{sd}} > 0} &\propto |eV_{\text{sd}}| \pm \frac{\delta_{>}}{2}, \quad \delta_{>} \approx \frac{2\sigma(\theta-1)}{\theta-\sigma-2} \Delta, \\ \ln \left. \frac{dI}{dV_{\text{sd}}} \right|_{V_{\text{sd}} < 0} &\propto |eV_{\text{sd}}| \pm \frac{\delta_{<}}{2}, \quad \delta_{<} \approx \frac{2\sigma(\theta-1)}{\theta-\sigma+2\theta\sigma} \Delta, \end{aligned} \quad (2)$$

Here, "+" is used for Mo<sup>t</sup>S<sup>b</sup> bilayer stacking and "-" for S<sup>t</sup>Mo<sup>b</sup>, showing that Mo<sup>t</sup>S<sup>b</sup> stacking promotes tunneling for both directions of the applied bias, whereas S<sup>t</sup>Mo<sup>b</sup> stacking demotes tunneling, which is a result of lack of mirror asymmetry in the device architecture (Fig. 1). The size of the bias offsets,  $\delta_{>}/e$  and  $\delta_{<}/e$ , between the I(V) characteristics for the two FE states of MoS<sub>2</sub> bilayer is parametrized using the following characteristics of the two materials:

$$\sigma = \frac{d_{\text{BN}} \epsilon_{\text{MoS}}}{d_{\text{MoS}} \epsilon_{\text{BN}}}, \quad \theta = \frac{d_{\text{MoS}}}{d_{\text{BN}}} \sqrt{\frac{m_{\text{MoS}} U_{\text{BN}}^3}{m_{\text{BN}} U_{\text{MoS}}^3}}.$$

Here,  $d_{\text{MoS}} = 12.3 \text{ \AA}$  and  $d_{\text{BN}} = 3 \times 3.33 \text{ \AA} = 9.99 \text{ \AA}$  are the thicknesses of the corresponding layers, while  $\epsilon_{\text{BN}} \approx 3$  and  $\epsilon_{\text{MoS}} \approx 6.2$  are their dielectric permittivities<sup>32-34</sup>, hence,  $\sigma \approx 1.68$ . Without knowledge of the precise values of the band offsets and effective masses, we can assess the qualitative features of the I(V) characteristics such as the bias voltage asymmetry. In this regards, eq. (2) shows a systematic difference between the bias offsets (due to the FE polarization of the MoS<sub>2</sub> bilayer) for positive and negative voltages. In particular, in the case of  $\theta \gg 1$ , expected for  $|U_{\text{BN}}| \gg U_{\text{MoS}}$  and  $m_{\text{MoS}} \sim -m_{\text{BN}} \sim m_0$ , we find that  $\delta_{>} \approx 231 \text{ meV} > \delta_{<} \approx 48 \text{ meV}$  in general agreement with the experiment (Fig. 2c).

Having understood the effect of polarisation switching in single-domain tunnelling structures, we study devices fabricated of marginally twisted MoS<sub>2</sub> bilayers where local lattice reconstruction leads to a periodic triangular domain layout (type 2). Such devices show a much smaller hysteresis,  $\delta/e \leq 50 \text{ mV}$  (regardless of the bias voltage sweep range), Fig.3a. This indicates that while the domain network does experience some changes due to expansion/contraction of Mo<sup>t</sup>S<sup>b</sup>/S<sup>t</sup>Mo<sup>b</sup> areas, complete switching cannot be achieved, since both types of polarisation are present in the tunnelling area at all times. This complies with the earlier observed transformations of domains/domain wall networks in marginally twisted MoS<sub>2</sub> bilayers, where it was noted that the networks of domain walls

separating areas with opposite FE polarisation have a higher rigidity in bilayers with shorter moiré periods, and nodes of such networks are essentially pinned<sup>35,36</sup> due to  $C_3$  symmetry of the acting forces.

Similar behaviour is observed in a sample where two domain walls are present and connected to an adjacent intersection, Fig.3b. In this sample, however, the tunnelling junction was defined not only in graphene, but also etched into the  $\text{MoS}_2$  bilayer, removing the ferroelectric material around the junction. While we can only see the initial domain configuration, we expect the domain configuration to be pinned at the boundary of the tunnelling area due to the etching process, known to introduce a substantial damage in the vicinity of the edge<sup>37</sup>. Therefore, the partial dislocation cannot be fully expelled from the sample. Similar pinning behaviour was recently observed on other structural defects, such as cracks, edges and contamination<sup>20,38</sup>.

The application of ferroelectric materials in electronic devices depends on one's ability to control their polarisation state. The above-discussed examples of FE switching/hysteresis behaviour all include tunnel junctions defined over areas which contain both  $\text{Mo}'\text{S}^b$  and  $\text{S}'\text{Mo}^b$  domains, so that the repolarisation of the structure was possible due to the motion/deformation of the pre-existing domain walls. Note that these domain walls are nothing but partial dislocations in rhombohedral layered crystals and are examples of topologically stable defects. For comparison, we also investigated tunnelling through single polarisation domain areas of  $\text{MoS}_2$  bilayer, both pristine and pierced by one perfect (full) dislocation (Fig.3c). In the fabrication of such devices, we used a 7L hBN tunnelling barrier enabling application of a higher electric bias for a wider range control of the ferroelectric state. However, despite applying stronger out-of-plane electric fields up to 0.85 V/nm, we systematically do not observe any hysteresis in the measurements. This behaviour qualitatively differs from the observations made on conventional FE materials, such as  $\text{Pb}(\text{Zr,Ti})\text{O}_3$  and  $\text{BaTiO}_3$  where nucleation of domains with inverted FE polarisation was observed<sup>39,40</sup> in electric fields as low as  $\sim 0.01$  V/nm.

We attribute this difference in behaviour to the “sliding nature” of the polarisation switching, specific to van der Waals systems with interfacial ferroelectricity<sup>14–17</sup>, which leads to a high energy cost of domain walls determined by straining each  $\text{MoS}_2$  monolayer near the domain boundary. This can be estimated as nucleation of an isolated circular seed of  $\text{S}'\text{Mo}^b$  stacking inside a  $\text{Mo}'\text{S}^b$  domain (case (i) in Fig. 3(e)). Such seed will have a critical radius when it becomes energetically favourable,  $r = w_{avg}/EP$ , determined by  $w_{avg} = 1.305$  eV/nm, the orientation-averaged domain wall energy per unit length<sup>29</sup> and  $E$ , the repolarising field. Such critical nucleation radius would be smaller,  $r = (w_{avg} - u_*/\pi)/EP$ , for a seed initiated at a perfect dislocation (case (ii) in Fig. 3(e), characterised<sup>29</sup> by an energy per unit length of  $u_* = 2.24$  eV/nm). Alternatively, one can imagine repolarisation to happen via unzipping a perfect dislocation in a pair of parallel partial dislocations (case (iii) in Fig. 3(e)):



which would have energetically unfavourable orientations with energy per unit length  $w_* = 1.13$  eV/nm. This determines the critical width for the repolarised stripe as  $r = (2w_* - u_*)/2EP$ . The above three scenarios of a critical seed formation are illustrated in Fig. 3(d) to show that forming a seed with size comparable to twice a typical domain wall width would require a high field,  $E \sim 1$  eV/nm.

Potentially, seeding the inverted polarisation may be promoted at the physical edge of the MoS<sub>2</sub> bilayer. One option is that a repolarised domain forms as a stripe (case (iv) in Fig. 3(e)) with the energy cost determined by a single domain wall energy. This energy cost would be minimised for a domain wall oriented following the armchair direction in the crystal,  $w = 0.96$  eV/nm, with the corresponding critical stripe width being  $r = w/2EP$ . This scenario is slightly less restrictive than the polarisation reversal inside a homogeneous domain. In a flake pierced by a full dislocation the nucleation of reversed polarisation appears to be even easier if it happens at the point where the full dislocation reaches the flake edge. As an estimate we consider an armchair edge with a perfect screw dislocation sticking along zigzag direction (case (v) in Fig. 3(e)). Then, the repolarisation seed unzips this dislocation, forming a triangular seed with sides oriented along the other two armchair axes (lowest energy direction for Mo<sup>t</sup>S<sup>b</sup>/S<sup>t</sup>Mo<sup>b</sup> domain wall). The energy of the triangular seed with a width  $r$  is  $-\frac{2}{\sqrt{3}}EP r^2 + 2w\frac{2r}{\sqrt{3}} - u_*r + \eta$ , where  $\eta$  characterises energies of stacking faults at the edge termination and merging site of individual dislocations. We note<sup>29</sup> that, accidentally,  $\frac{4w}{\sqrt{3}} \approx u_*$ , so that

we arrive at conditions for the critical seed size,  $r = \sqrt{\sqrt{3}\eta/2EP}$ , which are relaxed when compared to all the other cases, Fig. 4(d), over a broad range of energy  $\eta$ . Therefore, we conclude that crystal edges would play a major role in polarisation switching. Further investigations of the domain wall textures near the edges are required, as well as their dependence on crystallographic orientation, and functionalization or passivation of dangling bonds. To realise such studies, one would need to design a suitable device architecture that would avoid direct tunnelling currents near the R-TMD bilayer edge.

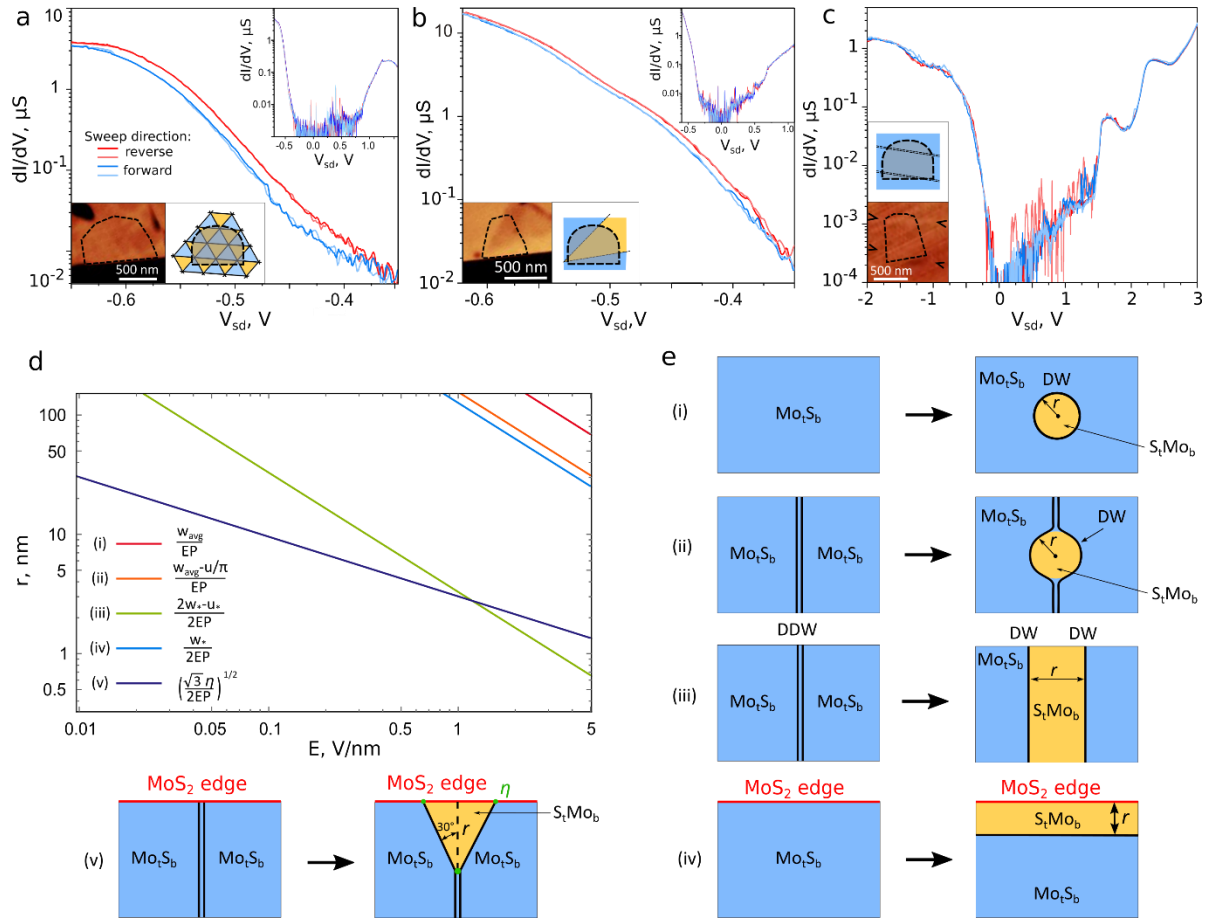


**Figure 3. Polarisation switching in FTJ with different domain layout and various nucleation scenarios.** Tunnelling conductance ( $dI/dV$ ) as a function of the transverse electric field ( $V_{sd}$ ) between the graphene source and the graphite drain for: (a) periodic triangular domain network ( $L \sim 60$ -150nm) (b) three domains with domain walls pinned at the edges of tunnelling area using RIE and (c) uniform domain area with two perfect dislocations crossing the studied region. Tunnelling hBN thickness is 2 layers (a, b), and 4 layers (c). This hysteresis is only observable for (a) and (b), reaching 17 mV in (a) and 7mV in (b) between the forward and reverse sweeps. For the devices in (a) and (b), the underlying hBN and R-MoS<sub>2</sub> were etched as well as the top graphene contact to eliminate the possible interaction between devices and the surrounding unbiased bilayer. All the results were acquired at  $T=1.5$  K. Insets show the pre-existing domain configuration visualised using friction AFM (left) and its schematic representation (right) with colour indicating domain polarisation (blue and yellow for in and out of plane) and solid lines showing dislocations. (d) Dependences of critical size of a reversal polarisation domain seed on out-of-plane electric field for five scenarios of nucleation shown in (e). In case (v) we estimated  $\eta = 0.04$  eV as configuration-averaged energy ( $\sim 0.4$  eV/nm<sup>2</sup>,<sup>41</sup>) of stacking fault with the area of MoS<sub>2</sub> monolayer unit cell.

## Methods:

**SPM domain mapping:** Electrical AFM techniques such as piezo-responsive force microscopy (PFM) and electrostatic force microscopy (EFM) were used. Here, equally high-domain-contrast was achieved using lateral/friction and tapping mode when conductive (budget sensors Multi-75G) probes were used.

**All electrical transport** measurements were performed at 1.5 K. When measuring the tunnelling conductance as a function of the transverse field, a sweeping DC bias with a constant small AC bias (1mV) were applied to the graphene source by a SR860 lock-in amplifier while A SR560 pre-amplifier was connected to the graphite drain to amplify the tunnelling current into a measurable voltage. The tunnelling conductance is defined as the ratio between the AC component of the tunnelling current and the AC bias applied by the lock-in. The AC amplitude applied on the graphene contacts was selected to be small enough compared to the DC bias but large enough to the thermal excitation (0.13meV) to guarantee the validity of the measurement.

1. Martin, L. W. & Rappe, A. M. Thin-film ferroelectric materials and their applications. *Nature Reviews Materials* **2**, 1–14 (2016).
2. Kim, Y. S. *et al.* Critical thickness of ultrathin ferroelectric BaTiO<sub>3</sub> films. *Appl. Phys. Lett.* **86**, 1–3 (2005).
3. Soni, R. *et al.* Giant electrode effect on tunnelling electroresistance in ferroelectric tunnel junctions. *Nat. Commun.* **5**, 1–10 (2014).
4. Wen, Z., Li, C., Wu, D., Li, A. & Ming, N. Ferroelectric-field-effect-enhanced electroresistance in metal/ferroelectric/semiconductor tunnel junctions. *Nat. Mater.* **12**, 617–621 (2013).
5. Yin, Y. W. *et al.* Multiferroic tunnel junctions. *Front. Phys.* **7**, 380–385 (2012).
6. Crassous, A. *et al.* Giant tunnel electroresistance with PbTiO<sub>3</sub> ferroelectric tunnel barriers. *Appl. Phys. Lett.* **96**, 10–13 (2010).
7. Qiao, H., Wang, C., Choi, W. S., Park, M. H. & Kim, Y. Ultra-thin ferroelectrics. *Materials Science and Engineering R: Reports* **145**, 100622 (2021).
8. Zhang, D., Schoenherr, P., Sharma, P. & Seidel, J. Ferroelectric order in van der Waals layered materials. *Nature Reviews Materials* **8**, 25–40 (2023).
9. Chang, K. *et al.* Discovery of robust in-plane ferroelectricity in atomic-thick SnTe. *Science* (80-. ). **353**, 274–278 (2016).
10. Yuan, S. *et al.* Room-temperature ferroelectricity in MoTe<sub>2</sub> down to the atomic monolayer limit. *Nat.*

- Commun.* **10**, 1–6 (2019).
11. Fei, Z. *et al.* Ferroelectric switching of a two-dimensional metal. *Nature* **560**, 336–339 (2018).
  12. de la Barrera, S. C. *et al.* Direct measurement of ferroelectric polarization in a tunable semimetal. *Nat. Commun.* **12**, 1–9 (2021).
  13. Liu, F. *et al.* Room-temperature ferroelectricity in CuInP<sub>2</sub>S<sub>6</sub> ultrathin flakes. *Nat. Commun.* **7**, 1–6 (2016).
  14. Vizner Stern, M. *et al.* Interfacial ferroelectricity by van der Waals sliding. *Science* (80-. ). **372**, 142–1466 (2021).
  15. Yasuda, K., Wang, X., Watanabe, K., Taniguchi, T. & Jarillo-Herrero, P. Stacking-engineered ferroelectricity in bilayer boron nitride. *Science* (80-. ). **372**, eabd3230 (2021).
  16. Woods, C. R. *et al.* Charge-polarized interfacial superlattices in marginally twisted hexagonal boron nitride. *Nat. Commun.* **12**, 1–7 (2021).
  17. Weston, A. *et al.* Interfacial ferroelectricity in marginally twisted 2D semiconductors. *Nat. Nanotechnol.* **17**, 390–395 (2022).
  18. Wang, X. *et al.* Interfacial ferroelectricity in rhombohedral-stacked bilayer transition metal dichalcogenides. *Nat. Nanotechnol.* 2022 174 **17**, 367–371 (2022).
  19. Deb, S. *et al.* Cumulative polarization in conductive interfacial ferroelectrics. *Nature* **612**, 465–469 (2022).
  20. Weston, A. *et al.* Interfacial ferroelectricity in marginally twisted 2D semiconductors. *Nat. Nanotechnol.* **17**, 390–395 (2022).
  21. Cui, X. *et al.* Multi-terminal transport measurements of MoS<sub>2</sub> using a van der Waals heterostructure device platform. *Nat. Nanotechnol.* **10**, 534–540 (2015).
  22. Britnell, L. *et al.* Strong light-matter interactions in heterostructures of atomically thin films. *Science* (80-. ). **340**, 1311–1314 (2013).
  23. Kim, K. *et al.* Van der Waals Heterostructures with High Accuracy Rotational Alignment. *Nano Lett.* **16**, 1989–1995 (2016).
  24. Uri, A. *et al.* Mapping the twist angle and unconventional Landau levels in magic angle graphene. (2019).
  25. Zhuravlev, M. Y., Wang, Y., Maekawa, S. & Tsymbal, E. Y. Tunneling electroresistance in ferroelectric tunnel junctions with a composite barrier. *Appl. Phys. Lett.* **95**, 1–4 (2009).
  26. Trainer, D. J. *et al.* Inter-Layer Coupling Induced Valence Band Edge Shift in Mono- to Few-Layer MoS<sub>2</sub>.

- Sci. Rep.* **7**, 1–11 (2017).
27. Castanon, E. G. *et al.* Calibrated kelvin-probe force microscopy of 2d materials using pt-coated probes. *J. Phys. Commun.* **4**, 1–13 (2020).
  28. Ferreira, F. *et al.* Weak ferroelectric charge transfer in layer-asymmetric bilayers of 2D semiconductors. *Sci. Rep.* **11**, 1–10 (2021).
  29. Enaldiev, V. V., Ferreira, F. & Fal'ko, V. I. A Scalable Network Model for Electrically Tunable Ferroelectric Domain Structure in Twistrionic Bilayers of Two-Dimensional Semiconductors. *Nano Lett.* **22**, 1534–1540 (2022).
  30. Tybell, T., Paruch, P., Giamarchi, T. & Triscone, J. M. Domain Wall Creep in Epitaxial Ferroelectric [Formula presented] Thin Films. *Phys. Rev. Lett.* **89**, 097601 (2002).
  31. *Tunneling Phenomena in Solids. Tunneling Phenomena in Solids* (Springer US, 1969). doi:10.1007/978-1-4684-1752-4
  32. Koo, J., Gao, S., Lee, H. & Yang, L. Vertical dielectric screening of few-layer van der Waals semiconductors. *Nanoscale* **9**, 14540–14547 (2017).
  33. Laturia, A., Van de Put, M. L. & Vandenberghe, W. G. Dielectric properties of hexagonal boron nitride and transition metal dichalcogenides: from monolayer to bulk. *npj 2D Mater. Appl.* **2**, 1–7 (2018).
  34. Ferreira, F., Enaldiev, V. V. & Fal'ko, V. I. Scaleability of dielectric susceptibility  $\epsilon_{zz}$  with the number of layers and additivity of ferroelectric polarization in van der Waals semiconductors. *Phys. Rev. B* **106**, 125408 (2022).
  35. Molino, L. *et al.* Ferroelectric Switching at Symmetry-Broken Interfaces by Local Control of Dislocations Networks. *Adv. Mater.* 2207816 (2023). doi:10.1002/adma.202207816
  36. Halbertal, D. *et al.* Moiré metrology of energy landscapes in van der Waals heterostructures. *Nat. Commun.* **12**, 1–8 (2021).
  37. Cai, X. *et al.* Bridging the gap between atomically thin semiconductors and metal leads. *Nat. Commun.* **13**, 1–9 (2022).
  38. Ko, K. *et al.* Operando electron microscopy investigation of polar domain dynamics in twisted van der Waals homobilayers. *Nat. Mater.* **22**, 992–998 (2023).
  39. Kim, D. J. *et al.* Observation of inhomogeneous domain nucleation in epitaxial Pb (Zr,Ti) O<sub>3</sub> capacitors. *Appl. Phys. Lett.* **91**, 132903 (2007).
  40. Jo, J. Y. *et al.* Polarization switching dynamics governed by the thermodynamic nucleation process in ultrathin ferroelectric films. *Phys. Rev. Lett.* **97**, 247602 (2006).

41. Enaldiev, V. V., Zólyomi, V., Yelgel, C., Magorrian, S. J. & Fal'ko, V. I. Stacking Domains and Dislocation Networks in Marginally Twisted Bilayers of Transition Metal Dichalcogenides. *Phys. Rev. Lett.* **124**, 206101 (2020).